Monthly Notices of the ROYAL ASTRONOMICAL SOCIETY

MNRAS **00,** 1 (2022) https://doi.org/10.1093/mnras/stac2004

ExoMol line lists – XLVI. Empirical rovibronic spectra of silicon mononitrate (SiN) covering the six lowest electronic states and four isotopologues

Mikhail Semenov [1], Nicholas Clark,[1] Sergei N. Yurchenko [1], Gap-Sue Kim[2] and Jonathan Tennyson [1]★

[1]*Department of Physics and Astronomy, University College London, Gower Street, WC1E 6BT London, UK*
[2]*2Dharma College, Dongguk University, 30, Pildong-ro 1-gil, Jung-gu, Seoul 04620, Korea*

Accepted 2022 July 14. Received 2022 July 13; in original form 2022 June 19

ABSTRACT

Silicon mononitride ($^{28}Si^{14}N$, $^{29}Si^{14}N$, $^{30}Si^{14}N$, $^{28}Si^{15}N$) line lists covering infrared, visible, and ultraviolet regions are presented. The SiNful line lists produced by ExoMol include rovibronic transitions between six electronic states: $X\,^2\Sigma^+$, $A\,^2\Pi$, $B\,^2\Sigma^+$, $D\,^2\Delta$, $a\,^4\Sigma^+$, $b\,^4\Pi$. The *ab initio* potential energy and coupling curves, computed at the multireference configuration interaction (MRCI/aug-cc-pVQZ) level of theory, are refined for the observed states by fitting their analytical representations to 1052 experimentally derived SiN energy levels determined from rovibronic bands belonging to the *X*–*X*, *A*–*X*, and *B*–*X* electronic systems through the MARVEL procedure. The SiNful line lists are compared to previously observed spectra, recorded and calculated lifetimes, and previously calculated partition functions. SiNful is available via the www.exomol.com database.

Key words: molecular data – opacity – astronomical data bases: miscellaneous – planets and satellites: atmospheres – stars: low-mass.

1 INTRODUCTION

Silicon is considered to be the second most abundant element in Earths crust (CRC Handbook 2016) and the seventh most abundant element on the planet, according to McDonough & Sun (1995); low silicon abundance within a host is considered to be a better indicator of a potential planet detection than planet-metallicity correlation, according to Brugamyer et al. (2011). So far, there have been multiple observations of silicon mononitrate (SiN) in different media in space: interstellar medium (Turner & Dalgarno 1977; Feldman et al. 1983; Schilke et al. 2003), red giant stars (Davis 1947; Gratton 1952), and envelopes of carbon stars (Turner 1992). Apart from being an important astrophysical species, SiN has multiple different applications: quantum dot production (Xie et al. 2017), quantum optomechanics (Serra et al. 2018), protective coating for biological tissues and dental implants (Pettersson et al. 2013; Raza et al. 2020), and membranes used in filtering and biosensor systems (Vlassiouk et al. 2009; Lee et al. 2014).

The SiN molecule seems to be well-studied experimentally in comparison to some of its valence group counterparts. Originally, the molecule was reported by Jevons (1913), with band heads attributed to the $B\,^2\Sigma^+$–$X\,^2\Sigma^+$ band. Later, Mulliken (1925) conducted a more thorough study of the $B\,^2\Sigma^+$–$X\,^2\Sigma^+$ reporting rotational transitions and detecting a weaker band later identified as $C\,^2\Pi$–$X\,^2\Sigma^+$ thanks to additional experimental works conducted by Linton (1975). Overall the main active electronic bands that have been rotationally resolved so far are $B\,^2\Sigma^+$–$X\,^2\Sigma^+$ (Jenkins & de Laszlo 1928; Stevens & Ferguson 1963; Schofield & Broida 1965; Nagaraj & Verma 1968; Dunn et al. 1969; Singh et al. 1973; Bredohl et al. 1976; Foster 1984; Walkup et al. 1984; Foster 1989; Piper & Caledonia 1991; Ito et al. 1993; Naulin et al. 1993; Ojha & Gopal 2013), $A\,^2\Pi$–$X\,^2\Sigma^+$ (Jevons 1913; Bredohl et al. 1976; Foster 1984; Foster, Lubic & Amano 1985; Yamada & Hirota 1985; Yamada et al. 1988; Foster 1989; Elhanine et al. 1992; Meloni et al. 2004), $C\,^2\Pi$–$X\,^2\Sigma^+$ (Mulliken 1925; Linton 1975; Bredohl et al. 1976; Foster 1989), and $B\,^2\Sigma^+$–$A\,^2\Pi$ (Bredohl et al. 1976). From these, Ojha & Gopal (2013) is the most recent experimental study, which apart from the $B\,^2\Sigma^+$–$X\,^2\Sigma^+$ band mentioned earlier, has also been able to detect and vibrationally resolve the $f\,^4\Sigma^-$–$d\,^4\Sigma^-$, $b\,^4\Pi$–$d\,^4\Sigma^-$. Additionally, we want to highlight that Nagaraj & Verma (1968) originally assigned their spectrum and quantum numbers to the SiO^+ anion, however, that was later corrected by the Dunn et al. (1969) and assigned to the $B\,^2\Sigma^+$–$X\,^2\Sigma^+$ band of SiN.

A large number of theoretical investigations of SiN have been performed since the discovery of the molecule (Gohel & Shah 1975; Preuss, Buenker & Peyerimhoff 1978; Bruna, Dohmann & Peyerimhoff 1984; Ziurys et al. 1984; Muller-Plathe & Laaksonen 1989; Curtiss et al. 1991; Melius & Ho 1991; Mclean, Liu & Chandler 1992; Chen, Krasowki & Fitzgerald 1993; Chong 1994; Borin 1996; Cai, Martin & Francois 1998; Singh et al. 1999; Jungnickel, Frauenheim & Jackson 2000; Kerkines & Mavridis 2005; Li et al. 2009; Oyedepo, Peterson & Wilson 2011; Xing et al. 2013, 2018). The most recent *ab initio* work at the time of writing was carried

★ E-mail: j.tennyson@ucl.ac.uk

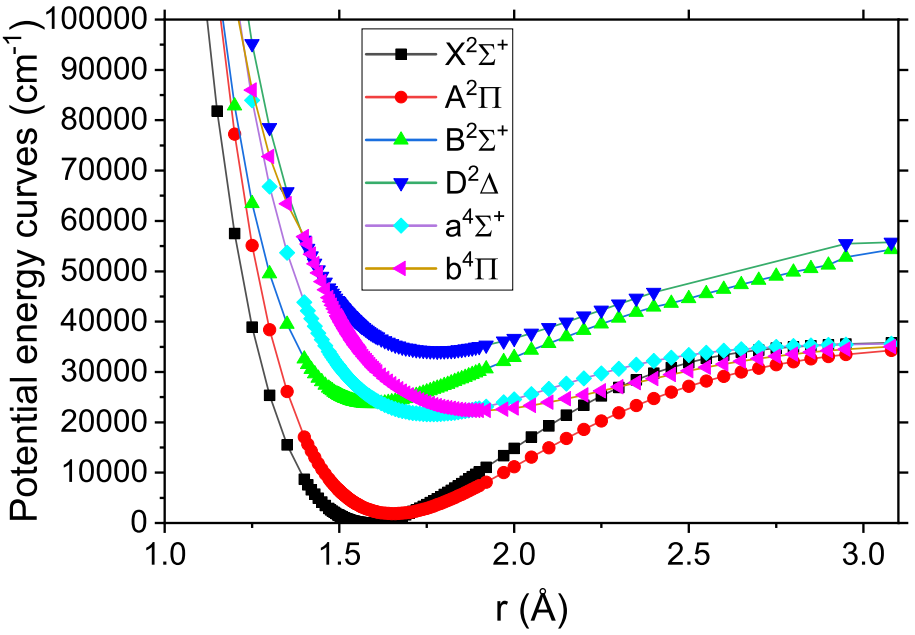

Figure 1. *Ab initio* PECs calculated at the icMRCI level of theory using aug-cc-pVQZ basis set. The grid was specifically made denser around the equilibrium points of the $X\,^2\Sigma^+$ and $A\,^2\Pi$ states.

out by Xing et al. (2018) who conducted a thorough analysis of the transition dipole moment curves (DMCs) and potential energy curves for the lowest eight doublets ($X\,^2\Sigma^+$, $A\,^2\Pi$, $B\,^2\Sigma^+$, $C\,^2\Pi$, $D\,^2\Delta$, $E\,^2\Delta$,$F\,^2\Pi$, $G\,^2\Delta$), of SiN, additionally reporting on Frank-Condon factors and lifetimes for the first 15 vibrational levels of each electronic state, for which they used program LEVEL due to Le Roy (1998). The states were studied at the Internally Contracted Multirefrence Configuration Interaction with Davidson correction (icMRCI + Q) level with additional extrapolation procedure employed as described by Oyeyemi et al. (2014). A lot of work in the 2018 paper was built on the foundation of their earlier paper (Xing et al. 2013), where they reported potential energy curves (PECs) for the lowest eight doublets ($X\,^2\Sigma^+$, $A\,^2\Pi$, $B\,^2\Sigma^+$, $C\,^2\Pi$, $D\,^2\Delta$, $E\,^2\Delta$, $F\,^2\Pi$, $G\,^2\Delta$) and four quartets ($a\,^4\Sigma^+$, $b\,^4\Pi$, $c\,^4\Delta$, $d\,^4\Sigma^-$) and the lowest sextet state $1^6\Sigma^+$. Apart form PECs, this paper also reported spectroscopic constants and discussed the effects of the spin–orbit couplings.

The work described below will present original *ab initio* PECs, spin–orbit curves (SOCs), electronic angular momentum curves (EAMCs) and (transition) DMCs calculated using a high-level of theory with MOLPRO (Werner et al. 2020) and then empirically fitted using data obtained from a measured active rotation vibration energy levels (MARVEL; Furtenbacher, Császár & Tennyson 2007) procedure and generated from effective Hamiltonians using PGOPHER (Western 2017). The refined spectroscopic model is then used to compute molecular line lists for four isotopologues of SiN. Both the refinement and line list calculations are performed using the rovibronic program DUO (Yurchenko et al. 2016). We then use our line lists to give high accuracy comparison to previously reported experimental spectra, calculated and experimental lifetimes, and partition function.

2 *Ab initio* MODEL

In this work, six lowest electronic states, namely $X\,^2\Sigma^+$, $A\,^2\Pi$, $B\,^2\Sigma^+$, $D\,^2\Delta$, $a\,^4\Sigma^+$, $b\,^4\Pi$, were studied using the state-averaged complete active space self-consistent field (CASSCF) and multireference configuration interaction (MRCI) methods and aug-cc-pVQZ basis sets. The calculations were performed using C_{2v} point group symmetry. Potential energy curves, illustrated in Fig. 1, spin–orbit coupling and electronic angular moment (Fig. 2), DMCs, and transition DMCs (Fig. 3) were computed using MOLPRO2020 (Werner et al. 2020). If the MOLPRO calculations at some geometries did not converge, they were interpolated or extrapolated from the neighbouring points as part of the rovibronic calculations (see below). We used an adaptive *ab initio* grid consisting of 121 bond lengths ranging from 1.1 to 3.08 Å with more points around the equilibrium region of the $X\,^2\Sigma^+$ state centred at 1.585 Å, see Figs 1–3, where the density of the *ab initio* grid is shown. The grid points with the corresponding *ab initio* values (if converged) are included in the supplementary material.

For *ab initio* calculation, we have considered the states of SiN correlating with two dissociation asymptotes, Si(^{3}P) + N(^{4}S) and Si(^{3}P) + N(^{2}D), which generate $^2\Sigma^+$(three states), $^2\Pi$ (one state), $^4\Sigma^+$(one states), and $^4\Pi$ (one state), which show six electronic states, $X\,^2\Sigma^+$, $A\,^2\Pi$, $B\,^2\Sigma^+$, $D\,^2\Delta$, $a\,^4\Sigma^+$, and $b\,^4\Pi$ that are mentioned above in *ab initio* model section. Under the C_{2v} point group symmetry, A_1 corresponds to Σ^+/Δ. Thus, the $^2\Delta$ state arose from the calculation of $^2\Sigma^+$. Molecular orbitals for the subsequent CI calculations were obtained for each spin and symmetry species from state averaged CASSCF calculations (Knowles & Werner 1985; Werner & Knowles 1985) where the state averaging was achieved over all six electronic states considered in this work.

Within the C_{2v} point group symmetry, 14 (8σ, $3\pi_x$, $3\pi_y$) orbitals which contained 6 closed (4σ, $1\pi_x$, $1\pi_y$) orbitals were used for all *ab initio* calculations. Thus, the active space represents 8 active (4σ, $2\pi_x$, $2\pi_y$) orbitals with 9 active electrons and spans the valence orbitals 5σ–8σ, 2π, 3π. All CI calculations were carried out with the internally contracted CI method (Knowles & Werner 1988; Werner & Knowles 1988). The CI calculations used the same set of reference configurations used in the CASSCF calculation.

The EAMCs represent the L_x and L_y matrix elements, which are important for the accurate description of the lambda doubling effects

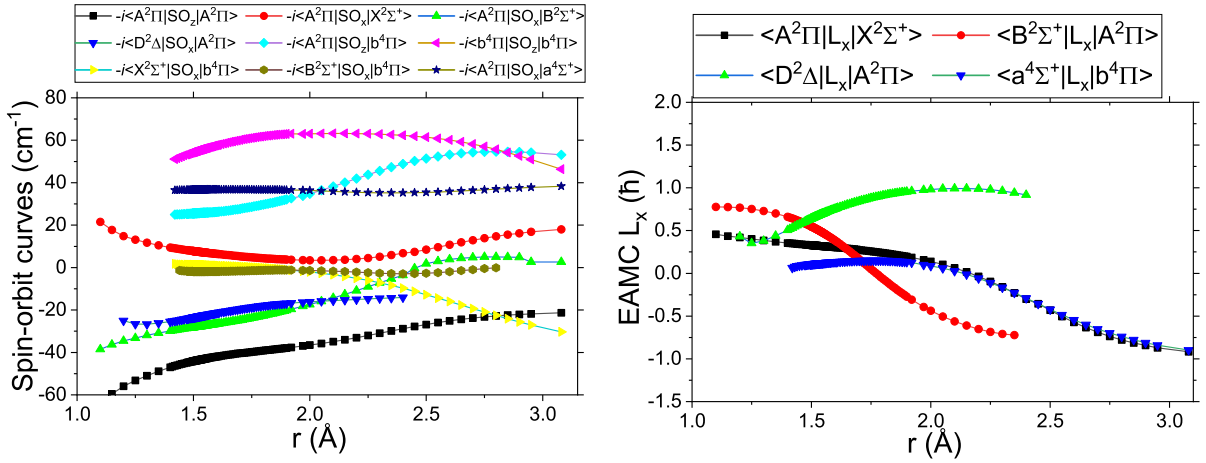

Figure 2. *Ab initio* coupling curves of SiN at the icMRCI/aug-cc-pVQZ level of theory. Left: spin–orbit matrix elements $\langle i|\mathrm{SO}|j\rangle$ for SiN at the icMRCI level of theory using aug-cc-pVQZ basis set. The MOLPRO values of the magnetic quantum numbers M_S (Σ) for the curves can be found in Table 1. Right: electronic angular momentum L_x curves.

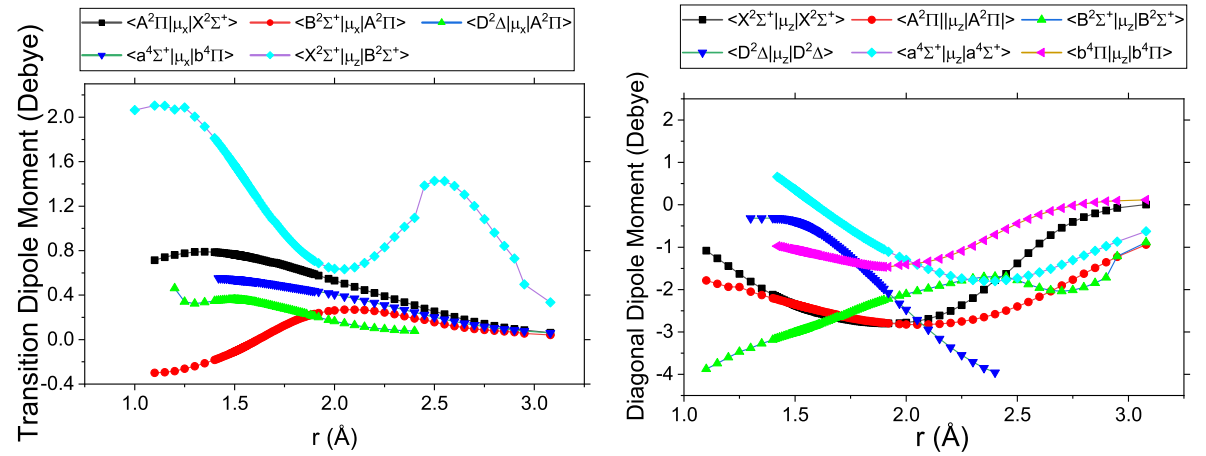

Figure 3. *Ab initio* transitional and diagonal DMCs calculated at the icMRCI level of theory using aug-cc-pVQZ basis set.

Table 1. MOLPRO magnetic quantum numbers M_S values (also known as Σ, projection of $\hat{\mathbf{S}}$ along the body fixed z-axis) for the *ab initio* spin–orbit matrix elements displayed in Fig. 2.

SOC	bra M_S	ket M_S
$\langle A\,^2\Pi_y\|\mathrm{SO}_x\|X\,^2\Sigma^+\rangle$	−0.5	0.5
$\langle A\,^2\Pi_y\|\mathrm{SO}_x\|B\,^2\Sigma^+\rangle$	−0.5	0.5
$\langle A\,^2\Pi_y\|\mathrm{SO}_x\|a\,^4\Sigma^+\rangle$	−0.5	0.5
$\langle D\,^2\Delta_{xy}\|\mathrm{SO}_x\|A\,^2\Pi_y\rangle$	−0.5	0.5
$\langle X\,^2\Sigma^+\|\mathrm{SO}_x\|b\,^4\Pi_y\rangle$	0.5	-0.5
$\langle B\,^2\Sigma^+\|\mathrm{SO}_x\|b\,^4\Pi_y\rangle$	0.5	-0.5
$\langle A\,^2\Pi_x\|\mathrm{SO}_z\|A\,^2\Pi_x\rangle$	0.5	0.5
$\langle A\,^2\Pi_x\|\mathrm{SO}_z\|b\,^4\Pi_x\rangle$	0.5	0.5
$\langle b\,^4\Pi_x\|\mathrm{SO}_z\|b\,^4\Pi_x\rangle$	0.5	0.5

in Π states originating from the interactions with the Σ and Δ states. In Fig. 2 (right), the L_x components are shown, with L_y related to them by symmetry.

The definition of SOCs, which help form a complete and self-consistent description of a spectroscopic model, requires knowledge of the magnetic quantum numbers M_S (i.e. the projection of the electronic spin Σ), which are specified in Table 1.

All of the *ab initio* curves are later mapped to a different, denser grid used in the solution of the rovibronic problem via interpolation and extrapolation as described in the Spectroscopic Model section below.

The (transition) DMCs $A\,^2\Pi$–$X\,^2\Sigma^+$, $B\,^2\Sigma^+$–$X\,^2\Sigma^+$, $B\,^2\Sigma^+$–$A\,^2\Pi$, $D\,^2\Delta$–$A\,^2\Pi$, $a\,^4\Sigma^+$–$b\,^4\Pi$, and DMCs $X\,^2\Sigma^+$–$X\,^2\Sigma^+$, $A\,^2\Pi$–$A\,^2\Pi$, $B\,^2\Sigma^+$–$B\,^2\Sigma^+$, $D\,^2\Delta$–$D\,^2\Delta$, $a\,^4\Sigma^+$–$a\,^4\Sigma^+$, and $b\,^4\Pi$–$b\,^4\Pi$ were calculated *ab initio* at the same level of theory as the PECs and are shown in Fig. 3. The phases of these non-diagonal TDMCs were selected to be consistent with the phases of the *ab initio* curves produced in our MOLPRO calculations (Patrascu et al. 2014). There is a discontinuity in $\langle X\,^2\Sigma^+|\mu_x|B\,^2\Sigma^+\rangle$ at 2.5 Å that we attribute to the interaction with the higher electronic states, which are not included in this model. Due to the large displacement from the equilibrium corresponding to very high energies, this discontinuity does not provide any material effect on our results, as can be seen from the spectra reproduced below.

3 MARVEL

All available experimental transition frequencies of SiN were extracted from the published spectroscopic literature and analysed using the MARVEL procedure (Császár et al. 2007; Furtenbacher

Table 2. Breakdown of the assigned transitions by electronic bands for the sources used in this MARVEL study. A and V are the numbers of the available and validated transitions, respectively. The mean and maximum uncertainties (Unc.) obtained using the MARVEL procedure are given in cm^{-1}.

Electronic band	Vibrational bands	J Range	A/V	WN range cm^{-1}	Unc. (Mean/Max)
29JeDeXX					
$B\,^2\Sigma^+$–$X\,^2\Sigma^+$	(0,0),(1,1),(2,2),(3,2),(3,3)	0.5–43.5	1060/1355	23267–24279	0.100/0.197
	(4,3),(4,4),(5,4),(5,5),(6,5)	0.5–43.5			
68NaVexx					
$B\,^2\Sigma^+$–$X\,^2\Sigma^+$	(0,0),(1,1),(2,2)	0.5–44.5	420/422.0	23876–24280	0.030/0.191
76BrDuHo					
$B\,^2\Sigma^+$–$X\,^2\Sigma^+$	(1,0),(2,0)	0.5–1.5	4/4	25236–26203	0.100/0.100
84YaHiXX					
$A\,^2\Pi$–$X\,^2\Sigma^+$	(0,0)	0.5–31.5	195/195	1918–2037	0.007/0.007
85FoLuAm $A\,^2\Pi$–$X\,^2\Sigma^+$	(1,0)	0.5–36.5	199/199	2917–3039	$0.001/1.00 \times 10^{-3}$
$X\,^2\Sigma^+$–$X\,^2\Sigma^+$	(0,0)	0.5–4.5	6/6	2.9039–5.8329	$1.00 \times 10^{-3}/1.00 \times 10^{-3}$
92ElHaGu $X\,^2\Sigma^+$-$X\,^2\Sigma^+$	(1,0),(2,0)	0.5–1.5	4/4	1140–2267	0.100/0.100

et al. 2007; Furtenbacher & Császár 2012; Tóbiás et al. 2019). This procedure takes a set of assigned transition frequencies with measurement uncertainties and converts it into a consistent set of empirical energy levels with the uncertainties propagated from the input transitions. The transition data extracted as part of this work from the literature covers the three main bands of SiN involving the $X\,^2\Sigma^+$, $A\,^2\Pi$, and $B\,^2\Sigma^+$ electronic states: $X\,^2\Sigma^+$–$X\,^2\Sigma^+$, $A\,^2\Pi$–$X\,^2\Sigma^+$, and $B\,^2\Sigma^+$–$X\,^2\Sigma^+$, as summarized in Table 2.

3.1 Description of experimental sources

All the available sources of experimental transitions considered in this work are listed below:

92ElHaGu by Elhanine et al. (1992): an infrared (IR) study of the $A\,^2\Pi$–$X\,^2\Sigma^+$ system through 724 transitions. Unfortunately, the original line data with assignments were lost/unavailable and only the derived spectroscopic constants for $A\,^2\Pi$ and $X\,^2\Sigma^+$ states remain. Using their $X\,^2\Sigma^+$ constants, we produced four $X\,^2\Sigma^+$–$X\,^2\Sigma^+$ pseudo-experimental lines (MARVEL Magic numbers) to help connecting spectroscopic networks in the MARVEL analysis. We also used their extended set of the spectroscopic constants in PGOPHER (Western 2017) to generate pseudo-experimental energies for the first five vibrational states of $A\,^2\Pi$ and the first three vibrational states of $X\,^2\Sigma^+$ states (up to $J = 49.5$) for the refinement of our spectroscopic model (see below). Elhanine et al. (1992) is the only existing information on the vibrationally excited $A\,^2\Pi$ states of SiN and is therefore crucial for providing MARVEL energies for states of $A\,^2\Pi$ with $v > 1$. The PGOPHER file used to generate the energies for fitting is provided as part of the supplementary information.

85FoLuAm by Foster et al. (1985): This IR observation reported 187 lines of the $A\,^2\Pi$–$X\,^2\Sigma^+$ system originally assigned to the (2,0) band and 6 microwave transitions in the $X\,^2\Sigma^+$–$X\,^2\Sigma^+$ system. This band was later reassigned to 1–0 by Yamada et al. (1988).

85YaHiXX by Yamada & Hirota (1985): This IR study reported 170 lines of the $A\,^2\Pi$–$X\,^2\Sigma^+$ system originally assigned to the (1,0) band, which, however, was later reassigned to (0,0) by Yamada et al. (1988).

76BrDuHo by Bredohl et al. (1976): This is a UV study of the $B\,^2\Sigma^+$–$X\,^2\Sigma^+$ system. Only spectroscopic constants were reported, which we used to generate four pseudo-experimental $B\,^2\Sigma^+$–$X\,^2\Sigma^+$ lines using PGOPHER to help connect the MARVEL inputs into a single spectroscopic network with $J' = 1.5$ $B\,^2\Sigma^+ \longleftarrow J'' = 0.5$ $A\,^2\Pi$ for the (1,0) and (2,0) bands (*e* and *f*).

75Linton by Linton (1975): This UV study reported 460 lines of the $C\,^2\Pi$–$A\,^2\Pi$ system. Sadly due to the low quality of this data and the lack of information provided in the paper to reconstruct the full set of quantum numbers required for MARVEL, this source is omitted from the MARVEL analysis of the current work, but the original lines scanned using OPTICAL CHARACTER READER software are still provided as part of the supplementary information.

68NaVe by Nagaraj & Verma (1968): This UV study reported 422 lines of the $B\,^2\Sigma^+$–$X\,^2\Sigma^+$ system covering the (0,0), (1,1), and (2,2) bands. Originally the spectra were assigned to the SiO^+ molecules, but were reassigned to SiN later as per the correction in Dunn et al. (1969).

29JeDe by Jenkins & de Laszlo (1928): This 1929 work is still the most extensive to date UV observation of the $B\,^2\Sigma^+$–$X\,^2\Sigma^+$ system of SiN reporting 1355 lines from the (0,0), (1,1), (2,2), (3,3), (4,4), (3,2), (4,3), (5,4), and (6,5) vibronic bands.

In total, 1987 experimental and 9 pseudo-experimental transitions were processed via the online MARVEL app (available through a user-friendly web interface at http://kkrk.chem.elte.hu/marvelonline) using the Cholesky (analytic) approach with a 0.5 cm^{-1} threshold on the uncertainty of the 'very bad' lines. The final MARVEL process for $^{28}Si^{14}N$ resulted in one main spectroscopic network, containing 1054 energy levels and 1456 validated transitions, with the rotational excitation up to $J = 44.5$ and covering energies up to 30 308 cm^{-1}. These energy levels in conjunction with energies generated from PGOPHER were used to refine our *ab initio* rovibronic spectroscopic model (PECs, SOCs, and EAMCs) presented above. The MARVEL input transitions and output energy files are given as part of the supplementary material.

4 ROVIBRONIC CALCULATIONS

To obtain rovibronic energies and wavefunctions for the six electronic states in question, we solve a set of fully coupled Schrödinger equation for the motion of nuclei using the DUO program (Yurchenko et al. 2016). DUO uses the Hunds case a basis set with the vibrational basis functions obtained by solving uncoupled vibrational Schrödinger equations for each electronic state in question with using a sinc DVR basis set (Guardiola & Ros 1982). Atomic masses are used to represent the kinetic energy operator. In DUO calculations, an equidistant grid of 501 radial points ranging from 1.1 to 5.0 Å. The *ab initio* curves were cubic-spline interpolated to map the *ab initio* curves on to the denser DUO grid. For the extension outside the *ab initio* bond lengths ($r > 3.080$ Å), the *ab initio* curves were extrapolated using the functional forms given by (Yurchenko et al.

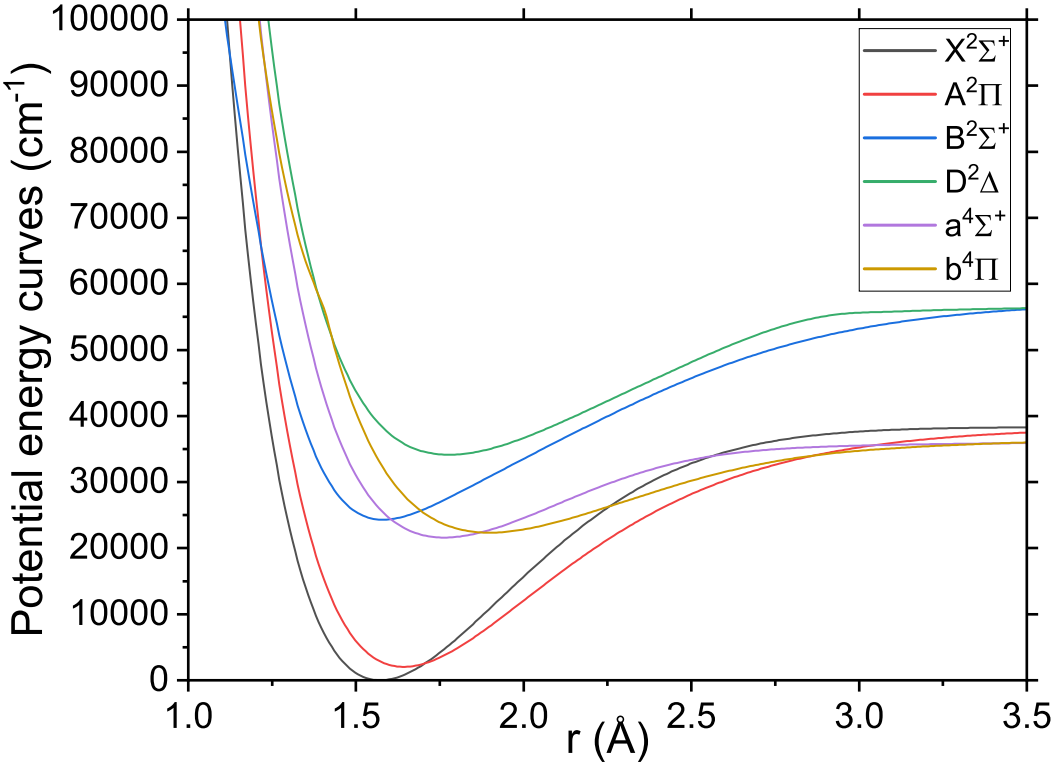

Figure 4. Potential energy curves of SiN representing our final spectroscopic and used in the DUO calculations: $X\,^2\Sigma^+$, $A\,^2\Pi$, and $B\,^2\Sigma^+$ are refined while $D\,^2\Delta$, $a\,^4\Sigma^+$, and $b\,^4\Pi$ are *ab initio*.

2016)

$$\begin{aligned} f^{\rm short}_{\rm PEC}(r) &= A + B/r, \\ f^{\rm short}_{\rm TDMC}(r) &= Ar + Br^2, \\ f^{\rm short}_{\rm other}(r) &= A + Br, \end{aligned} \tag{1}$$

for short-range and

$$\begin{aligned} f^{\rm long}_{\rm PEC}(r) &= A + B/r^6 \\ f^{\rm long}_{\rm EAMC}(r) &= A + Br, \\ f^{\rm long}_{\rm other}(r) &= A/r^2 + B/r^3 \end{aligned} \tag{2}$$

for long-range, where A and B are stitching parameters. A more detailed description of the DUO methodology was previously given by Yurchenko et al. (2016), see also Tennyson et al. (2016b).

4.1 Refining the spectroscopic model

For our spectroscopic model of SiN, we initially used *ab initio* PECs for the doublets $X\,^2\Sigma^+$, $A\,^2\Pi$, $B\,^2\Sigma^+$, $D\,^2\Delta$ and quartets $b\,^4\Pi$, $a\,^4\Sigma^+$, as well as all appropriate SOCs and EAMCs of SiN. The $X\,^2\Sigma^+$, $A\,^2\Pi$, and $B\,^2\Sigma^+$PECs and the associated couplings were then refined by fitting to our empirical set of MARVEL and PGOPHER term values of ^{28}Si^{14}N as described above.

For the refinements, the PECs for the $X\,^2\Sigma^+$, $A\,^2\Pi$, and $B\,^2\Sigma^+$ states were parametrized using the extended morse oscillator function (Lee et al. 1999) as given by

$$V(r) = V_{\rm e} + (A_{\rm e} - V_{\rm e})\left[1 - \exp\left(-\sum_{k=0}^{N} B_k \xi_p^k (r - r_{\rm e})\right)\right]^2, \tag{3}$$

where $A_{\rm e} - V_{\rm e} = D_{\rm e}$ is the dissociation energy, $A_{\rm e}$ is the corresponding asymptote, $r_{\rm e}$ is an equilibrium distance, and ξ_p is the Šurkus variable (Šurkus, Rakauskas & Bolotin 1984) given by

$$\xi_p = \frac{r^p - r_{\rm e}^p}{r^p + r_{\rm e}^p} \tag{4}$$

with $V_{\rm e} = 0$ for the $X\,^2\Sigma^+$ state. The $X\,^2\Sigma^+$ and $A\,^2\Pi$ states have a common asymptote, which was fixed for the analytical form of the potential to the ground-state dissociation energy $D_{\rm e}$ 4.75 eV based on the experiment by Naulin et al. [1993; see also Kerkines & Mavridis (2005)]. Similarly the $B\,^2\Sigma^+$ state was adjusted to be 19 233 cm^{-1} above the $X\,^2\Sigma^+$ dissociation using the atomic excitation energy of N (Kramida et al. 2021). The processed and refined PECs used in DUO can be seen in Fig. 4.

For the parametrization of SOCs and the EAMCs, the *ab initio* curves were morphed using a polynomial decay expansion as given by:

$$F(r) = \sum_{k=0}^{N} B_k\, z^k (1 - \xi_p) + \xi_p\, B_\infty, \tag{5}$$

where z is the damped-coordinate polynomial given by:

$$z = (r - r_{\rm ref})\, e^{-\beta_2 (r - r_{\rm ref})^2 - \beta_4 (r - r_{\rm ref})^4}. \tag{6}$$

The refined curves $f(r)$ are the represented as

$$f(r) = F(R) f^{\rm ai}(r),$$

with $B_\infty = 1$ in order for $F(r) \to 1$ at $r \to \infty$. Morphing allows one to retain the original shape of the property with a minimum number of varied parameters, see e.g. Prajapat et al. (2017) and Yurchenko et al. (2018). In equation (6), $r_{\rm ref}$ is a reference position chosen to be close to $r_{\rm e}$ of $X\,^2\Sigma^+$ and β_2 and β_4 are damping factors, typically chosen to be 8×10^{-1} and 2×10^{-2}. The morphed and extended by DUO SOCs and EAMCs are shown in Fig. 5.

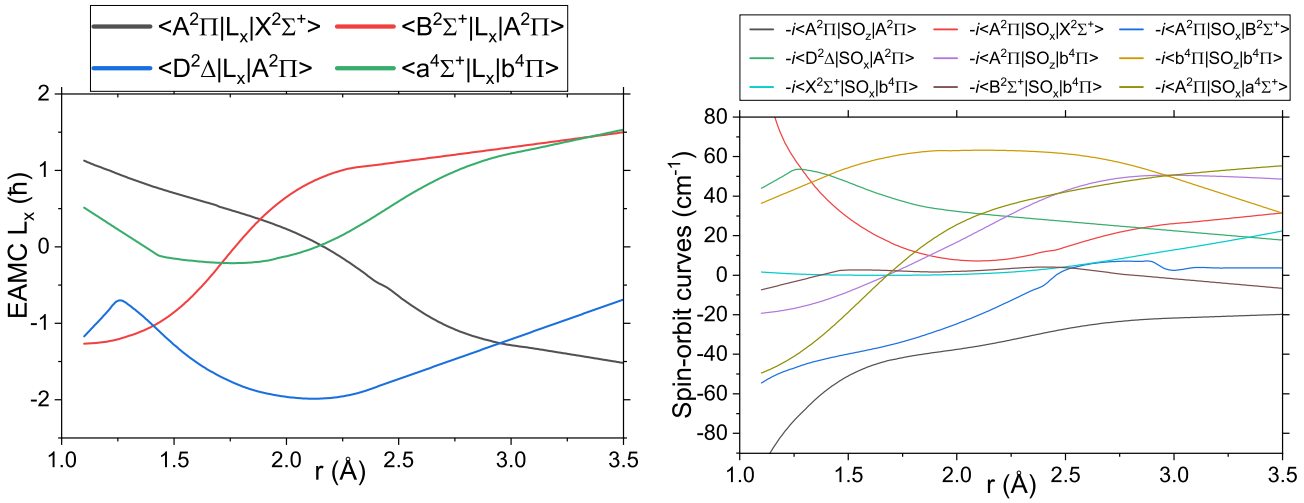

Figure 5. Refined electronic angular momentum and SOCs for SiN. The MOLPRO values of the magnetic quantum numbers M_S for the SOCs can be found in Table 1.

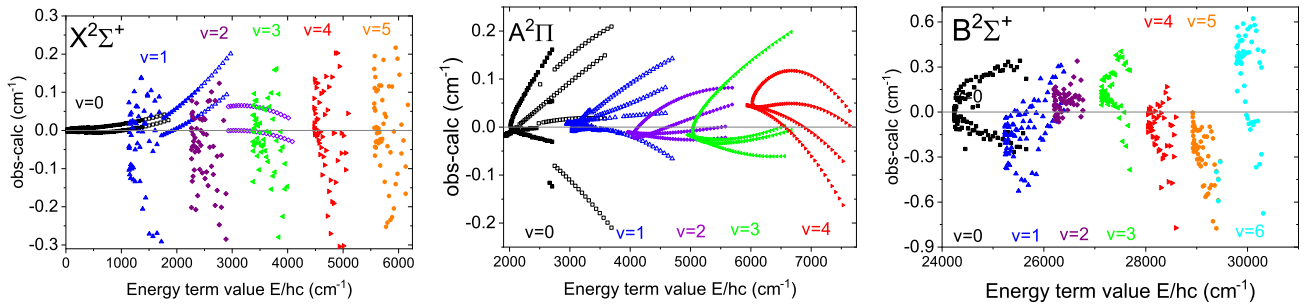

Figure 6. The residuals (Obs.-Calc.) between the experimentally determined energies of SiN ($X\,^2\Sigma^+$, $A\,^2\Pi$, and $B\,^2\Sigma^+$) from our MARVEL analysis (open), pseudo-experimental PGOPHER (filled) generated energies and DUO energies corresponding to our refined spectroscopic model. Only MARVEL energies are available for $B\,^2\Sigma^+$, hence the vibrational level labels are not differentiated by source.

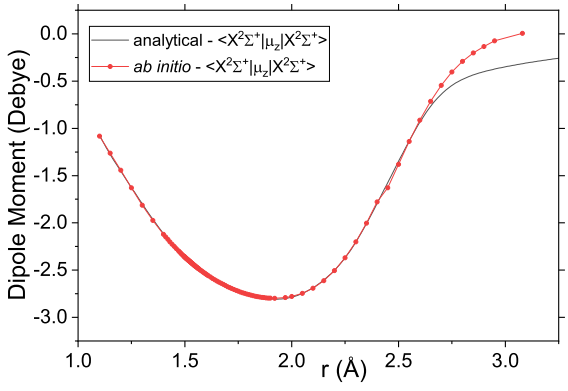

Figure 7. Comparison of the *ab initio* and fitted DMC for the $X\,^2\Sigma^+$–$X\,^2\Sigma^+$ system.

The 1062 MARVEL and 854 PGOPHER energy levels values were used to refine the PECs, SOCs, and EAMCs into analytical form as described above. Fig. 6 shows the residuals representing how well our model compares to the MARVEL and PGOPHER energies. Unfortunately, the most significant work from the number of transitions provided is Jenkins & de Laszlo (1928), where the accuracy of the transitions was 0.1 cm^{-1} at best. This is the main reason for the spread of uncertainties in the $X\,^2\Sigma^+$ and $B\,^2\Sigma^+$ states. Similarly most data for the $A\,^2\Pi$ state had to be supplemented using the PGOPHER calculations due to the difficulty of obtaining experimental data for the state.

4.2 Dipole moment curves

Most of the (transition) DMCs from Fig. 3 were left unchanged and used as grid points in DUO calculations apart from the $\langle X\,^2\Sigma^+|\mu_z|X\,^2\Sigma^+\rangle$, which was fitted to analytical form of the polynomial decay given in equation (5). Having an analytical form helps to reduce the numerical noise arising due to interpolation of *ab initio* curves present in high overtone transitions, see Medvedev et al. (2016). The comparison between *ab initio* $X\,^2\Sigma^+$–$X\,^2\Sigma^+$ DMC and its analytical form is shown in Fig. 7, with the deviations at very large radial displacement not affecting the intensities for the energy excitations selected for this study.

All expansion parameters or curves defining our spectroscopic model are given as supplementary material to the paper as a DUO input file.

5 LINE LIST AND SIMULATIONS OF SPECTRA OF SIN

The SiNful line list was produced with DUO using the empirically refined and *ab initio* curves as described above. For the main

Table 3. Line list statistics for each isotopologue of SiN.

Isotopologue	g_{ns}	N_{states}	N_{trans}
$^{28}Si^{14}N$	3	131935	43646806
$^{29}Si^{14}N$	6	132335	43946969
$^{30}Si^{14}N$	3	132706	44223730
$^{28}Si^{15}N$	2	133460	44816182

g_{ns}: nuclear spin degeneracy;
N_{states}: number of states;
N_{trans}: number of transitions.

isotopologue $^{28}Si^{14}N$, it contains 43 646 806 transitions and 131 935 states for $X\,^2\Sigma^+$, $A\,^2\Pi$, $B\,^2\Sigma^+$, $D\,^2\Delta$, $a\,^4\Sigma^+$, and $b\,^4\Pi$, covering wavenumbers up to 58 000 cm^{-1} $v = 0...30$ and $J = 0...245.5$. For the isotopologue line lists only the atomic masses were adjusted in the Duo input files. Further details on the line list statistics covering the isotpologues can be seen in Table 3. The line list is provided in State and Transition files, as is customary for the ExoMol format (Tennyson et al. 2020). Extracts from the States and Trans files are shown in Tables 4 and 5, respectively; the full files are available from www.exomol.com. The States file contains energy term values, state uncertainties, Landé-g factors (Semenov, Yurchenko & Tennyson 2017), lifetimes (Tennyson et al. 2016a), and quantum numbers. The Transition file contains Einstein A coefficients. The partition functions are also included as part of the standard line list compilation.

The calculated energies were replaced with the MARVEL values (MARVELized), where available. We have used the labels 'Ca','EH', and 'Ma' in the penultimate column of the States file to indicate if the energy value is calculated using Duo, derived using PGOPHER or MARVELized, respectively.

Table 5. An extract from the transitions file of the SiNful line list for $^{28}Si^{14}N$.

f	i	A_{fi} (s^{-1})	$\tilde{\nu}_{fi}$
34822	33867	6.3723E + 01	4047.041414
2808	2455	2.0314E-04	4047.041433
63044	62682	1.4457E-06	4047.041573
61850	60890	1.5342E-01	4047.042750
65187	65424	1.1950E + 02	4047.042900
75707	75959	2.7837E + 00	4047.043952
37830	36872	9.1146E-02	4047.044029
49826	49468	9.3588E-04	4047.044408
18065	18306	6.1554E + 01	4047.045440
53117	53365	5.3547E-02	4047.046876
70272	69910	5.1581E-03	4047.047010
106232	106467	5.6296E-01	4047.047815

f: upper state counting number;
i: lower state counting number;
A_{fi}: Einstein-A coefficient in s^{-1};
$\tilde{\nu}_{fi}$: transition wavenumber in cm^{-1}.

The uncertainty values in the States file correspond to two cases: the MARVEL uncertainties are used for MARVELized energies, while for the calculated values the following approximate expression is used:

$$\text{unc} = av + bJ(J+1), \tag{7}$$

where a and b are electronic state-dependent constant, given in Table 6. For the $X\,^2\Sigma^+$, $A\,^2\Pi$, and $B\,^2\Sigma^+$ states, uncertainties were estimated based on the progression of residuals from Fig. 6 as average increases of obs.-calc. in v and J for each state shown.

Table 4. An extract from the states file of the SiNful line list for $^{28}Si^{14}N$.

i	Energy (cm^{-1})	g_i	J	unc	τ	g	Parity	State	v	Λ	Σ	Ω	Label	Calc.
2	1138.471940	6	0.5	0.200000	0.5211	2.001919	+ e	X2Sigma +	1	0	0.5	0.5	Ma	1138.405398
3	2017.654928	6	0.5	0.010000	0.0015	0.000607	+ e	A2Pi	0	1	−0.5	0.5	Ma	2017.651598
4	2263.632470	6	0.5	0.400000	0.1714	2.000967	+ e	X2Sigma +	2	0	0.5	0.5	Ma	2263.834585
5	3037.121068	6	0.5	0.006000	0.0006	0.000570	+ e	A2Pi	1	1	−0.5	0.5	Ma	3037.120364
6	3375.983139	6	0.5	1.000000	0.0368	2.001071	+ e	X2Sigma +	3	0	0.5	0.5	Ma	3376.117442
7	4044.188981	6	0.5	0.200375	0.0004	0.000245	+ e	A2Pi	2	1	−0.5	0.5	EH	4044.208257
8	4475.345990	6	0.5	1.600000	0.0124	2.001414	+ e	X2Sigma +	4	0	0.5	0.5	Ma	4475.285785
9	5038.850133	6	0.5	0.300375	0.0003	−0.000102	+ e	A2Pi	3	1	−0.5	0.5	EH	5038.860507
10	5561.363517	6	0.5	0.100750	0.0057	2.001737	+ e	X2Sigma +	5	0	0.5	0.5	Ca	5561.363517
11	6021.067289	6	0.5	0.400375	0.0002	−0.000370	+ e	A2Pi	4	1	−0.5	0.5	EH	6021.017509
12	6634.354317	6	0.5	0.120750	0.0032	2.001917	+ e	X2Sigma +	6	0	0.5	0.5	Ca	6634.354317
13	6990.593938	6	0.5	0.500375	0.0002	−0.000488	+ e	A2Pi	5	1	−0.5	0.5	Ca	6990.593938
14	7694.239922	6	0.5	0.140750	0.0020	2.001777	+ e	X2Sigma +	7	0	0.5	0.5	Ca	7694.239922
15	7947.534233	6	0.5	0.600375	0.0002	−0.000299	+ e	A2Pi	6	1	−0.5	0.5	Ca	7947.534233
16	8740.963173	6	0.5	0.160750	0.0014	2.000443	+ e	X2Sigma +	8	0	0.5	0.5	Ca	8740.963173
17	8891.787413	6	0.5	0.700375	0.0001	0.001068	+ e	A2Pi	7	1	−0.5	0.5	Ca	8891.787413

i: state counting number.
$\tilde{E}$: state energy term values in cm^{-1}.
g_i: total statistical weight, equal to $g_{ns}(2J+1)$.
J: total angular momentum.
unc: uncertainty, cm^{-1}.
τ: lifetime (s^{-1}).
g: Landé g-factors.
+/ −: Total parity.
State: electronic state.
v: state vibrational quantum number.
Λ: projection of the electronic angular momentum.
Σ: projection of the electronic spin.
Ω: projection of the total angular momentum, $\Omega = \Lambda + \Sigma$.
Label: 'Ma' is for MARVEL,'EH' is PGOPHER generated and 'Ca' is for Calculated (using Duo).

Table 6. *a* and *b* constants (cm^{-1}) defining state-dependent uncertainties via equation (7).

State	*a*	*b*
$X\,^2\Sigma^+$	0.02	0.001
$A\,^2\Pi$	0.1	0.001
$B\,^2\Sigma^+$	0.5	0.001
All other	0.8	0.001

5.1 Overall spectra

To demonstrate the accuracy of the SiNful line list, several spectra were calculated, analysed, and compared to available laboratory measurements. Fig. 8 illustrates the main bands of SiN at 2000 K. The dominance of the $X\,^2\Sigma^+$–$A\,^2\Pi$ in the 0–5000 cm^{-1} region confirms why it is hard to detect the comparatively weak $X\,^2\Sigma^+$–$X\,^2\Sigma^+$ transitions. Additionally, while the $X\,^2\Sigma^+$–$B\,^2\Sigma^+$ band system appears to be overall stronger than $A\,^2\Pi$– $B\,^2\Sigma^+$, the latter should still be detectable in the 18 000–24 000 cm^{-1} region according to our model, in line with observations of these vibronic bands by Ojha & Gopal (2006) and Foster et al. (1985). Additionally, in the region above 28 000 cm^{-1}, the $A\,^2\Pi$ -$D\,^2\Delta$ band becomes dominant, which agrees with previous vibronic observations in this region by Bredohl et al. (1976). Fig. 9 shows how the spectrum of $^{28}Si^{14}N$ changes with increasing temperature.

5.2 $B\,^2\Sigma^+$–$X\,^2\Sigma^+$ band

$B\,^2\Sigma^+$–$X\,^2\Sigma^+$ is the strongest electronic band in the system, with the largest number of experimental observations due to it being the easiest to detect. In Fig. 10, we simulate the $B\,^2\Sigma^+$–$X\,^2\Sigma^+$ (5,4) and (4,3) band at rotational temperature of 392 and 412 K, respectively, to provide direct comparison with the experiment. The simulated spectra is also adjusted to be in air rather than in vacuum to align with the experimental spectra. This is achieved by using the IAU standard of conversion adopted by Morton (1991):

$$\lambda_{air} = \frac{\lambda_{vacuum}}{(1.0 + 2.735182 \times 10^{-4} + \frac{131.4182}{\lambda_{vac}^2} + \frac{2.76249\times^8}{\lambda_{vac}^4})} \quad (8)$$

where λ_{air} and λ_{vac} are wavelengths in air and vacuum, respectively. The overall agreement on the rotational structure is within the uncertainty provided.

5.3 $A\,^2\Pi$–$X\,^2\Sigma^+$ band

The $A\,^2\Pi$–$X\,^2\Sigma^+$ band system was first detected by Jevons (1913), however, because of the vicinity of the $A\,^2\Pi$ and $X\,^2\Sigma^+$ states it has proved difficult to study experimentally. Fig. 11 shows the comparison of our simulated spectra of the $A\,^2\Pi$–$X\,^2\Sigma^+$ (1,0) band with the experiment of Foster et al. (1985). The spectrum is simulated at the effective temperature of 740 K. The position of the bands agrees to 0.05 cm^{-1}, which is within our calculated uncertainties.

Fig. 12 shows a comparison of the simulated spectra (shown as sticks) for different silicon isotopes of the SiN molecule with the experimental spectra of Yamada et al. (1988). The overall agreement for $^{28}Si^{14}Nis$ ∼0.016 cm^{-1}, for $^{29}Si^{14}N$ is ∼0.035 cm^{-1}, and for $^{30}Si^{14}N$ is ∼0.055 cm^{-1}. The intensities were adjusted based on the natural abundance for each silicon isotope. These are defined as 92.2 per cent, 4.68 per cent, and 3.09 per cent for $^{28}Si^{14}N$,$^{29}Si^{14}N$, and $^{30}Si^{14}N$, respectively. Additionally, in the same range, a $Q_{22}(0.5)$ line of $A\,^2\Pi$–$X\,^2\Sigma^+$ (0,0) for $^{29}Si^{14}N$ should be present, but it was probably too weak to be observed during the experiment. This line is indicated with an asterisk.

5.4 Lifetimes

There are few precise experimental measurements of the lifetimes of different electronic states of SiN in the literature. Walkup et al.

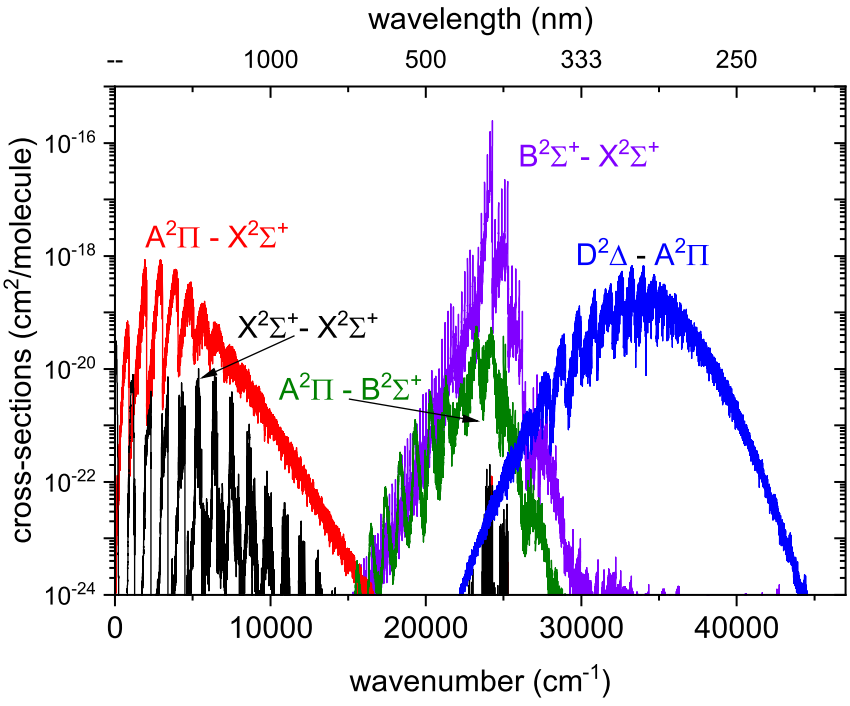

Figure 8. Simulated absorption spectrum of SiN at 2000 K showing the main bands of the system. A Gaussian profile of the half width of half maximum (HWHM) of 1 cm^{-1} was used.

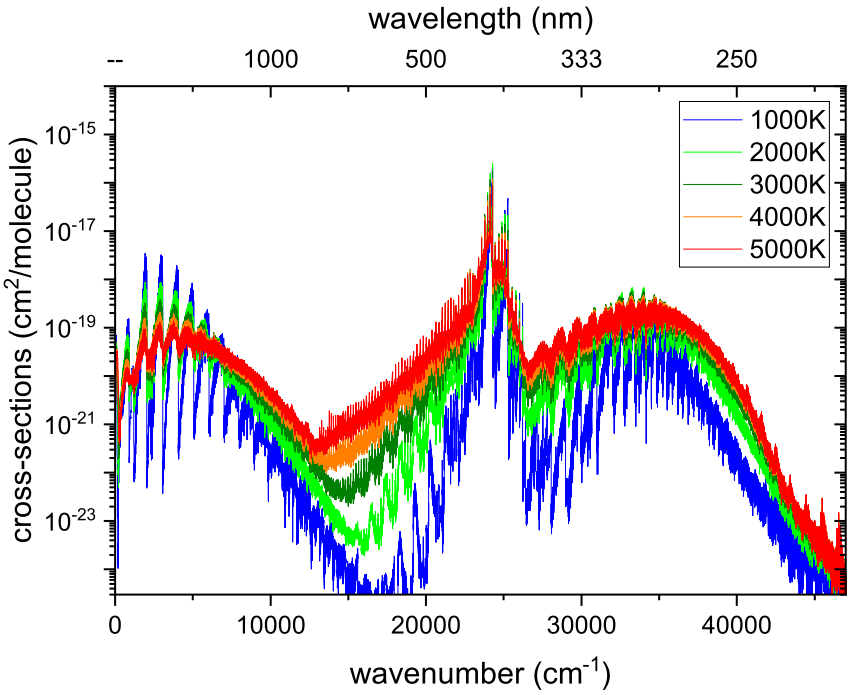

Figure 9. Temperature dependence of the SiN spectra using the SiNful line list. A Gaussian profile with HWHM of 1 cm^{-1} was used.

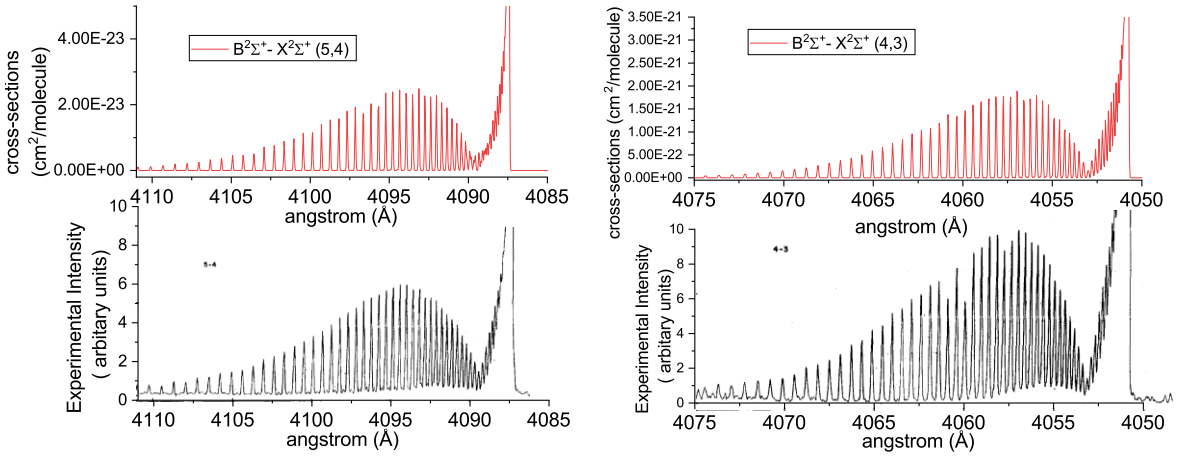

Figure 10. Simulated absorption spectra of SiN showing the $B\,^2\Sigma^+$–$X\,^2\Sigma^+$ (5,4) and (4,3) bands at temperature of 392 and 412 K, respectively. A comparison to the experimental spectra from Schofield & Broida (1965) is provided. A Gaussian profile HWHM of 0.2 cm^{-1} was used.

(1984) report the $B\,^2\Sigma^+$ $v = 1$ vibrational state to have a lifetime of 200 ns ±10 ns ($T_{\rm rot}$ = 500 K). Our calculated value for this vibronic state is lower: 130 ns ($J = 0.5$), slowly increasing to 150 ns for $J =$ 100 ns and even 200 ns for $J = 160.5$ ($v = 1$, $B\,^2\Sigma^+$). Additionally, there have been several theoretical works (Kaur & Baluja 2015; Xing et al. 2018) which showed that for the $A\,^2\Pi$ state the lifetimes decrease with the vibrational levels as lower levels are much less energetically accessible due to the proximity of the $X\,^2\Sigma^+$ state. This can be seen in more detail in Table 7, where we compare our calculated lifetimes with those of Xing et al. (2018); the agreement is good.

5.5 Partition function

For the partition function of $^{28}Si^{14}N$, we follow the ExoMol and HITRAN (Gamache et al. 2017) convention and include the full nuclear spin. This means that our convention is different to that of recently reported by Barklem & Collet (2016) with whom we compare our results in Fig. 13. In order for comparison to be in equivalent convention, their partition function was multiplied by the factor of three as ^{14}N has a nuclear spin degeneracy of 3 and ^{28}S has nuclear spin degeneracy of 0. The differences at higher temperatures can be attributed to incompleteness of the model used by Barklem & Collet (2016), which is demonstrated by comparing partition functions by using only $X\,^2\Sigma^+$ state, $X\,^2\Sigma^+$ and $A\,^2\Pi$ states, and all states: the partition function of Barklem & Collet (2016) appears to be based on the $X\,^2\Sigma^+$ state only. As evident from Fig. 13, the contribution from the $A\,^2\Pi$ state cannot be neglected due to its low-excitation energy.

Partition functions in for $T = 1$–3000 K in steps of 1 K are available the four isotopologue, $^{28}Si^{14}N$, $^{29}Si^{14}N$, $^{30}Si^{14}N$, and $^{28}Si^{15}N$, are available via the ExoMol website.

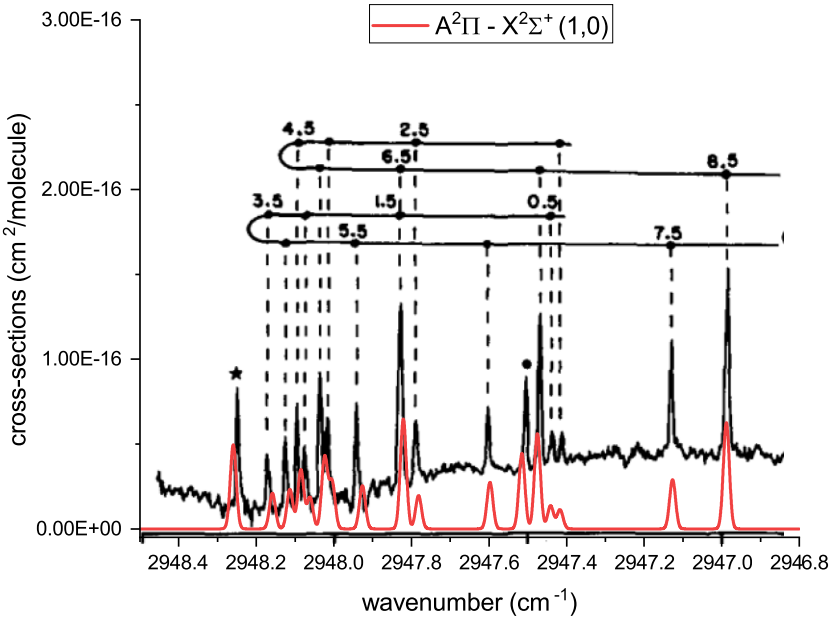

Figure 11. Simulated absorption spectrum of SiN at effective temperature of 740 K showing the $A\,^2\Pi$–$X\,^2\Sigma^+$ (1,0) band. A Gaussian profile of HWHM of 0.009 cm^{-1} was used. A comparison with the experimental spectra from Foster et al. (1985) is provided, with calculated spectra in red and experimental in black.

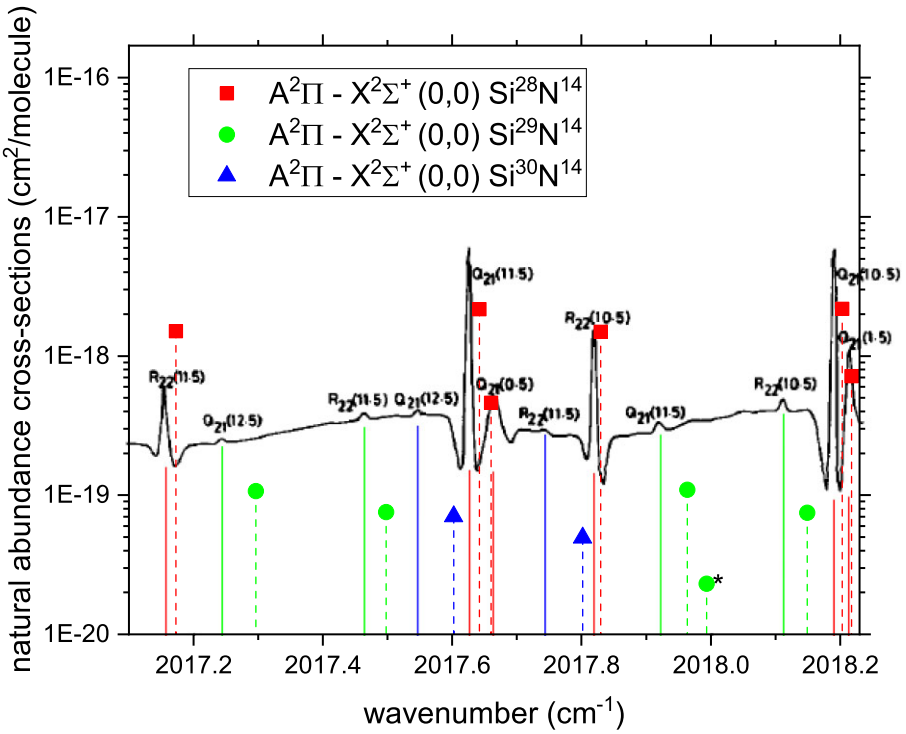

Figure 12. Comparison of the simulated stick spectrum and experimental emission spectrum of the SiN isotpologues ($^{28}Si^{14}N$, $^{29}Si^{14}N$, $^{30}Si^{14}N$) at 300 K. Straight lines are experimentally observed line positions and dashed lines with points represent calculated. The asterisk indicates the $Q_{22}(0.5)$ line for $^{29}Si^{14}N$ not observed experimentally by (Yamada et al. 1988).

6 CONCLUSION

New IR and UV line lists called SiNful for isotopologues of SiN are presented. SiNful is available from www.exomol.com (Tennyson et al. 2020) and www.zenodo.org (European Organization For Nuclear Research & OpenAIRE 2013). As part of the line list construction, a MARVEL analysis for $^{28}Si^{14}N$ was performed. All experimental line positions from the literature (to the best of our knowledge) currently available for the *X*–*X*, *A*–*X* and *B*–*X* systems were processed to generate a MARVEL set of empirical energies of SiN. An accurate spectroscopic model for SiN was built: *ab initio* (T)DMC and empirically refined PECs, SOCs, EAMCs, using

Table 7. Comparison of lifetimes from our current work (A) and Xing et al. (2018) (B). An experimental lifetime 200 ± 10 ns was reported by Walkup et al. (1984) for $v' = 1$ of $B\,^2\Sigma^+$.

	$A\,^2\Pi$/ μs		$B\,^2\Sigma^+$/ ns	
v'	A	B	A	B
0	1460	1660	124	129
1	610	679	130	136
2	385	429	137	143
3	281	312	143	150
4	221	245	150	157
5	182	202	156	164
6	155	172	163	170
7	135	149	169	176
8	121	132	175	181
9	109	119	181	187
10	98.3	109	186	192
11	90.5	99.8	192	196
12	84.0	92.6	197	201
13	78.5	86.6	202	205
14	73.9	81.5	207	210

both previously derived MARVEL energies as well as PGOPHER generated energies.

The line list was MARVELized, where the theoretical energies are replaced with the MARVEL values (where available). The line list provides uncertainties of the rovibronic states in order to help in high resolution applications. Comparisons of simulated spectra with experiment for both *A*–*X* and *B*–*X* system show close agreement. Additionally lifetimes, Landé-g factors, and partition functions are provided. The importance of inclusion of the energies of the excited state $A\,^2\Pi$ when computing the partition function of SiN is demonstrated.

ACKNOWLEDGEMENTS

This work was supported by UK STFC under grant ST/R000476/1 and the European Research Council (ERC) under the European Union's Horizon 2020 research and innovation programme through Advance Grant number 883830.

7 DATA AVAILABILITY

The data underlying this article are available in the article and in its online supplementary material, including (1) the DUO input files for each isotopologue containing all the potential energy, (transition) dipole moment, and coupling curves of SiN used in this work, (2) the MARVEL data set, (3) digitalized line data from Linton (1975), (4) extracted ab initio curves as part of the excel, (5) PGOPHER file used to generate energy levels for two low-lying states, (6) the temperature-dependent partition function of $^{28}Si^{14}N$ up to 10 000 K. The SiNful line lists for $^{28}Si^{14}N$, $^{29}Si^{14}N$, $^{30}Si^{14}N$, and $^{28}Si^{15}N$ are available from www.exomol.com.

REFERENCES

Barklem P. S., Collet R., 2016, A&A, 588, A96
Borin A., 1996, Chem. Phys. Lett., 262, 80
Bredohl H., Dubois I., Houbrechts Y., Singh M., 1976, Can. J. Phys., 54, 680
Brugamyer E., Dodson-Robinson S. E., Cochran W. D., Sneden C., 2011, ApJ, 738, 97
Bruna P., Dohmann H., Peyerimhoff S., 1984, Can. J. Phys., 62, 1508
Cai Z., Martin J., Francois J., 1998, J. Mol. Spectrosc., 188, 27
Chen H., Krasowki M., Fitzgerald G., 1993, J. Chem. Phys., 98, 8710
Chong D., 1994, Chem. Phys. Lett., 220, 102
CRC Handbook, 2016, CRC Handbook of Chemistry and Physics, 88th Edition, 97 edn. CRC Press
Császár A. G., Czakó G., Furtenbacher T., Mátyus E., 2007, Annu. Rep. Comput. Chem., 3, 155
Curtiss L. A., Raghavachari K., Trucks G. W., Pople J. A., 1991, J. Chem. Phys., 94, 7221
Davis D., 1947, AJ, 106, 28

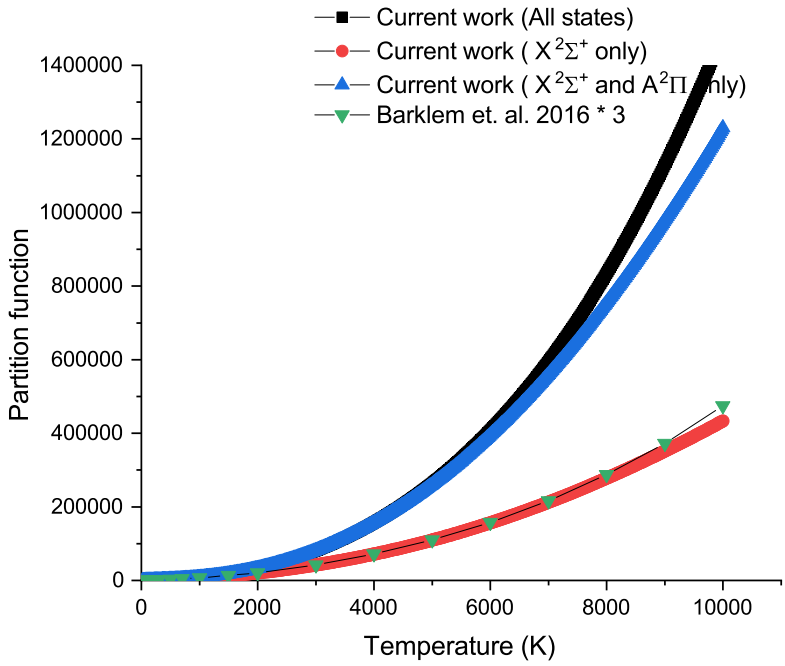

Figure 13. Comparison of the partition functions for $^{28}Si^{14}N$: values from this work and the work of Barklem & Collet (2016).

Dunn T. M., Rao K. M., Nagaraj S., Verma R. D., 1969, Can. J. Phys., 47, 2128
Elhanine M., Hanoune B., Guelachvili G., Amiot C., 1992, J. Phys. II, 2, 931
European Organization For Nuclear Research OpenAIRE, 2013, Zenodo https://www.zenodo.org/
Feldman P., Matthews H., Bell M., Herzberg G., Saito S., Endo Y., Hirota E., 1983, J. R. Astron. Soc. Can., 77, 258
Foster S., 1984, J. Mol. Spectrosc., 106, 369
Foster S., 1989, J. Mol. Spectrosc., 137, 430
Foster S., Lubic K., Amano T., 1985, J. Chem. Phys., 82, 709
Furtenbacher T., Császár A. G., 2012, J. Mol. Struct., 1009, 123
Furtenbacher T., Császár A. G., Tennyson J., 2007, J. Mol. Spectrosc., 245, 115
Gamache R. R. et al., 2017, J. Quant. Spectrosc. Radiat. Transf., 203, 70
Gohel V., Shah N., 1975, Indian J. Pure Appl. Phys., 13, 162
Gratton L., 1952, AJ, 115, 346
Guardiola R., Ros J., 1982, J. Chem. Phys., 45, 374
Ito H., Suzuki K., Kondow T., Kuchitsu K., 1993, Chem. Phys. Lett., 208, 328
Jenkins F., de Laszlo H., 1928, Proc. R. Soc., 122, 103
Jevons W., 1913, Proc. R. Soc., 89, 187
Jungnickel G., Frauenheim T., Jackson K., 2000, J. Chem. Phys., 112, 1295
Kaur S., Baluja K. L., 2015, Eur. Phys. J. D, 69, 89
Kerkines I., Mavridis A., 2005, J. Chem. Phys., 123, 124301
Knowles P. J., Werner H.-J., 1985, Chem. Phys. Lett., 115, 259
Knowles P. J., Werner H.-J., 1988, Chem. Phys. Lett., 145, 514
Kramida A., Ralchenko Y., Reader J., NIST ASD Team, 2021, NIST Atomic Spectra Database (ver. 5.9), [Online]. Available: http://physics.nist.gov/asd [2021, October 31]. National Institute of Standards and Technology, Gaithersburg, MD.
Le Roy R. J., 1998, J. Mol. Spectrosc., 191, 223
Lee D.-s., Song H.-W., Choi C.-G., Jung M. Y., 2014, J. Biomed. Opt., 19, 1
Lee E. G., Seto J. Y., Hirao T., Bernath P. F., Le Roy R. J., 1999, J. Mol. Spectrosc., 194, 197
Li B.-X., Wang G.-y., Ding W.-f., Ren X.-j., Ye J.-z., 2009, Phys. B: Condens. Matter, 404, 1679
Linton C., 1975, J. Mol. Spectrosc., 55, 108
McDonough W., Sun S.-s., 1995, Chem. Geol., 120, 223
Mclean A., Liu B., Chandler G., 1992, J. Chem. Phys., 97, 8459
Medvedev E. S., Meshkov V. V., Stolyarov A. V., Ushakov V. G., Gordon I. E., 2016, J. Mol. Spectrosc., 330, 36
Melius C., Ho P., 1991, J. Phys. Chem., 95, 1410
Meloni G., Sheehan S., Ferguson M., Neumark D., 2004, J. Phys. Chem. A, 108, 9750
Morton D. C., 1991, ApJS, 77, 119
Muller-Plathe F., Laaksonen L., 1989, Chem. Phys. Lett., 160, 175
Mulliken R., 1925, Phys. Rev., 26, 0319
Nagaraj S., Verma R. D., 1968, Can. J. Phys., 46, 1597
Naulin C., Costes M., Moudden Z., Ghanem N., Dorthe G., 1993, Chem. Phys. Lett., 202, 452
Ojha K. S., Gopal R., 2006, Indian J. Phys., 80, 819
Ojha K. S., Gopal R., 2013, Spectra Chim. Acta A, 109, 155
Oyedepo G. A., Peterson C., Wilson A. K., 2011, J. Chem. Phys., 135, 094103
Oyeyemi V. B., Krisiloff D. B., Keith J. A., Libisch F., Pavone M., Carter E. A., 2014, J. Chem. Phys., 140, 044317
Patrascu A. T., Hill C., Tennyson J., Yurchenko S. N., 2014, J. Chem. Phys., 141, 144312
Pettersson M., Tkachenko S., Schmidt S., Berlind T., Jacobson S., Hultman L., Engqvist H., Persson C., 2013, J. Mech. Behav. Biomed. Mater., 25, 41
Piper L. G., Caledonia G. E., 1991, J. Chem. Phys., 95, 698
Prajapat L., Jagoda P., Lodi L., Gorman M. N., Yurchenko S. N., Tennyson J., 2017, MNRAS, 472, 3648
Preuss R., Buenker R., Peyerimhoff S., 1978, J. Mol. Spectrosc., 49, 171
Raza S. M., Khurshid Z., Zafar M. S., Najeeb S., Ul Yaqin S. A., 2020, in Zafar M. S., Khurshid Z., Khan A. S., Najeeb S., Sefat F., eds, Woodhead Publishing Series in Biomaterials, Dental Implants. Woodhead Publishing, p. 287
Schilke P., Leurini S., Menten K., Alcolea J., 2003, A&A, 412, L15
Schofield K., Broida H. P., 1965, Photochem. Photobiol., 4, 989
Semenov M., Yurchenko S. N., Tennyson J., 2017, J. Mol. Spectrosc., 330, 57
Serra E. et al., 2018, J. Microelectromech. Syst., 27, 1193
Singh M., Bredohl H., Remy F., Dubois I., 1973, J. Phys. B: At. Mol. Opt. Phys., 6, 2656
Singh P., Sanzovo G., Borin A., Ornellas F., 1999, MNRAS, 303, 235
Stevens A., Ferguson H., 1963, Can. J. Phys., 41, 240
Šurkus A. A., Rakauskas R. J., Bolotin A. B., 1984, Chem. Phys. Lett., 105, 291
Tennyson J. et al., 2020, J. Quant. Spectrosc. Radiat. Transf., 255, 107228
Tennyson J., Hulme K., Naim O. K., Yurchenko S. N., 2016a, J. Phys. B: At. Mol. Opt. Phys., 49, 044002
Tennyson J., Lodi L., McKemmish L. K., Yurchenko S. N., 2016b, J. Phys. B: At. Mol. Opt. Phys., 49, 102001
Tóbiás R., Furtenbacher T., Tennyson J., Császár A. G., 2019, Phys. Chem. Chem. Phys., 21, 3473
Turner J., Dalgarno A., 1977, ApJ, 213, 386
Turner B. E., 1992, ApJ, 388, L35
Vlassiouk I., Apel P. Y., Dmitriev S. N., Healy K., Siwy Z. S., 2009, Proc. Natl. Acad. Sci., 106, 21039
Walkup R., Avouris P., Dreyfus R. W., Jasinski J. M., Selwyn G. S., 1984, Appl. Phys. Lett., 45, 372
Werner H.-J. et al., 2020, J. Chem. Phys., 152, 144107
Werner H.-J., Knowles P. J., 1985, J. Chem. Phys., 82, 5053
Werner H.-J., Knowles P. J., 1988, J. Chem. Phys., 89, 5803
Western C. M., 2017, J. Quant. Spectrosc. Radiat. Transf., 186, 221
Xie W. et al., 2017, Adv. Mater., 29, 1604866
Xing W., Shi D., Sun J., Zhu Z., 2013, Eur. Phys. J. D, 67, 228
Xing W., Shi D., Sun J., Zhu Z., 2018, ApJS, 237, 16
Yamada C., Hirota E., 1985, J. Chem. Phys., 82, 2547
Yamada C., Hirota E., Yamamoto S., Saito S., 1988, J. Chem. Phys., 88, 46
Yurchenko S. N., Lodi L., Tennyson J., Stolyarov A. V., 2016, Comput. Phys. Commun., 202, 262
Yurchenko S. N., Sinden F., Lodi L., Hill C., Gorman M. N., Tennyson J., 2018, MNRAS, 473, 5324
Ziurys L., Clemens D., Saykally R., Colvin M., Schaefer H., 1984, AJ., 281, 219

SUPPORTING INFORMATION

Supplementary data are available at *MNRAS* online.

Please note: Oxford University Press is not responsible for the content or functionality of any supporting materials supplied by the authors. Any queries (other than missing material) should be directed to the corresponding author for the article.

This paper has been typeset from a TEX/LATEX file prepared by the author.

List of astronomical key words (Updated on 2020 January)

This list is common to *Monthly Notices of the Royal Astronomical Society, Astronomy and Astrophysics*, and *The Astrophysical Journal*. In order to ease the search, the key words are subdivided into broad categories. No more than *six* subcategories altogether should be listed for a paper.

The subcategories in boldface containing the word 'individual' are intended for use with specific astronomical objects; these should never be used alone, but always in combination with the most common names for the astronomical objects in question. Note that each object counts as one subcategory within the allowed limit of six.

The parts of the key words in italics are for reference only and should be omitted when the keywords are entered on the manuscript.

General
editorials, notices
errata, addenda
extraterrestrial intelligence
history and philosophy of astronomy
miscellaneous
obituaries, biographies
publications, bibliography
sociology of astronomy
standards

Physical data and processes
acceleration of particles
accretion, accretion discs
asteroseismology
astrobiology
astrochemistry
astroparticle physics
atomic data
atomic processes
black hole physics
chaos
conduction
convection
dense matter
diffusion
dynamo
elementary particles
equation of state
gravitation
gravitational lensing: micro
gravitational lensing: strong
gravitational lensing: weak
gravitational waves
hydrodynamics
instabilities
line: formation
line: identification
line: profiles
magnetic fields
magnetic reconnection
(magnetohydrodynamics) MHD
masers
molecular data
molecular processes
neutrinos
nuclear reactions, nucleosynthesis, abundances
opacity
plasmas
polarization
radiation: dynamics
radiation mechanisms:general
radiation mechanisms: non-thermal
radiation mechanisms: thermal
radiative transfer
relativistic processes
scattering
shock waves
solid state: refractory
solid state: volatile
turbulence
waves

Astronomical instrumentation, methods and techniques
atmospheric effects
balloons
instrumentation: adaptive optics
instrumentation: detectors
instrumentation: high angular resolution
instrumentation: interferometers
instrumentation: miscellaneous
instrumentation: photometers
instrumentation: polarimeters
instrumentation: spectrographs
light pollution
methods: analytical
methods: data analysis
methods: laboratory: atomic
methods: laboratory: molecular
methods: laboratory: solid state
methods: miscellaneous
methods: numerical
methods: observational
methods: statistical
site testing
space vehicles
space vehicles: instruments
techniques: high angular resolution
techniques: image processing
techniques: imaging spectroscopy
techniques: interferometric
techniques: miscellaneous
techniques: photometric
techniques: polarimetric
techniques: radar astronomy
techniques: radial velocities
techniques: spectroscopic
telescopes

Astronomical data bases
astronomical data bases: miscellaneous
atlases
catalogues
surveys
virtual observatory tools

Software
software: data analysis
software: development
software: documentation
software: public release
software: simulations

Astrometry and celestial mechanics
astrometry
celestial mechanics
eclipses
ephemerides
occultations
parallaxes
proper motions
reference systems
time

The Sun
Sun: abundances
Sun: activity
Sun: atmosphere
Sun: chromosphere
Sun: corona
Sun: coronal mass ejections (CMEs)
Sun: evolution
Sun: faculae, plages
Sun: filaments, prominences
Sun: flares
Sun: fundamental parameters
Sun: general
Sun: granulation
Sun: helioseismology
Sun: heliosphere
Sun: infrared
Sun: interior
Sun: magnetic fields
Sun: oscillations
Sun: particle emission
Sun: photosphere
Sun: radio radiation
Sun: rotation
(Sun:) solar–terrestrial relations
(Sun:) solar wind
(Sun:) sunspots
Sun: transition region
Sun: UV radiation
Sun: X-rays, gamma-rays

Planetary systems
comets: general

comets: individual: . . .
Earth
interplanetary medium
Kuiper belt: general

Kuiper belt objects: individual: . . .
meteorites, meteors, meteoroids
minor planets, asteroids: general
minor planets, asteroids: individual: . . .
Moon
Oort Cloud
planets and satellites: atmospheres
planets and satellites: aurorae
planets and satellites: composition
planets and satellites: detection
planets and satellites: dynamical evolution and stability
planets and satellites: formation
planets and satellites: fundamental parameters
planets and satellites: gaseous planets
planets and satellites: general

planets and satellites: individual: . . .
planets and satellites: interiors
planets and satellites: magnetic fields
planets and satellites: oceans
planets and satellites: physical evolution
planets and satellites: rings
planets and satellites: surfaces
planets and satellites: tectonics
planets and satellites: terrestrial planets
planet–disc interactions
planet–star interactions
protoplanetary discs
zodiacal dust

Stars
stars: abundances
stars: activity
stars: AGB and post-AGB
stars: atmospheres
(stars:) binaries *(including multiple)*: close
(stars:) binaries: eclipsing
(stars:) binaries: general
(stars:) binaries: spectroscopic
(stars:) binaries: symbiotic
(stars:) binaries: visual
stars: black holes
(stars:) blue stragglers
(stars:) brown dwarfs
stars: carbon
stars: chemically peculiar
stars: chromospheres
(stars:) circumstellar matter
stars: coronae
stars: distances
stars: dwarf novae
stars: early-type
stars: emission-line, Be
stars: evolution
stars: flare
stars: formation
stars: fundamental parameters
(stars:) gamma-ray burst: general
(stars:) **gamma-ray burst: individual: . . .**
stars: general
(stars:) Hertzsprung–Russell and colour–magnitude diagrams
stars: horizontal branch
stars: imaging
stars: individual: . . .
stars: interiors

stars: jets
stars: kinematics and dynamics
stars: late-type
stars: low-mass
stars: luminosity function, mass function
stars: magnetars
stars: magnetic field
stars: massive
stars: mass-loss
stars: neutron
(stars:) novae, cataclysmic variables
stars: oscillations *(including pulsations)*
stars: peculiar *(except chemically peculiar)*
(stars:) planetary systems
stars: Population II
stars: Population III
stars: pre-main-sequence
stars: protostars
(stars:) pulsars: general
(stars:) **pulsars: individual: . . .**
stars: rotation
stars: solar-type
(stars:) starspots
stars: statistics
(stars:) subdwarfs
(stars:) supergiants
(stars:) supernovae: general
(stars:) **supernovae: individual: . . .**
stars: variables: Cepheids
stars: variables: Scuti
stars: variables: general
stars: variables: RR Lyrae
stars: variables: S Doradus
stars: variables: T Tauri, Herbig Ae/Be
(stars:) white dwarfs
stars: winds, outflows
stars: Wolf–Rayet

Interstellar medium (ISM), nebulae
ISM: abundances
ISM: atoms
ISM: bubbles
ISM: clouds
(ISM:) cosmic rays
(ISM:) dust, extinction
ISM: evolution
ISM: general
(ISM:) HII regions
(ISM:) Herbig–Haro objects

ISM: individual objects: . . .
(except planetary nebulae)
ISM: jets and outflows
ISM: kinematics and dynamics
ISM: lines and bands
ISM: magnetic fields
ISM: molecules
(ISM:) photodissociation region (PDR)
(ISM:) planetary nebulae: general
(ISM:) **planetary nebulae: individual: . . .**
ISM: structure
ISM: supernova remnants

The Galaxy
Galaxy: abundances
Galaxy: bulge
Galaxy: centre
Galaxy: disc
Galaxy: evolution
Galaxy: formation
Galaxy: fundamental parameters
Galaxy: general
(Galaxy:) globular clusters: general
(Galaxy:) **globular clusters: individual: . . .**
Galaxy: halo
Galaxy: kinematics and dynamics
(Galaxy:) local interstellar matter
Galaxy: nucleus
(Galaxy:) open clusters and associations: general
(Galaxy:) **open clusters and associations: individual: . . .**
(Galaxy:) solar neighbourhood
Galaxy: stellar content
Galaxy: structure

Galaxies
galaxies: abundances
galaxies: active
galaxies: bar
(galaxies:) BL Lacertae objects: general
(galaxies:) **BL Lacertae objects: individual: . . .**
galaxies: bulges
galaxies: clusters: general

galaxies: clusters: individual: . . .
galaxies: clusters: intracluster medium
galaxies: disc
galaxies: distances and redshifts
galaxies: dwarf
galaxies: elliptical and lenticular, cD
galaxies: evolution
galaxies: formation
galaxies: fundamental parameters
galaxies: general
galaxies: groups: general

galaxies: groups: individual: . . .
galaxies: haloes
galaxies: high-redshift

galaxies: individual: . . .
galaxies: interactions
(galaxies:) intergalactic medium
galaxies: irregular
galaxies: ISM
galaxies: jets
galaxies: kinematics and dynamics
(galaxies:) Local Group
galaxies: luminosity function, mass function
(galaxies:) Magellanic Clouds
galaxies: magnetic fields
galaxies: nuclei
galaxies: peculiar
galaxies: photometry
(galaxies:) quasars: absorption lines
(galaxies:) quasars: emission lines
(galaxies:) quasars: general

(galaxies:) **quasars: individual: . . .**
(galaxies:) quasars: supermassive black holes
galaxies: Seyfert
galaxies: spiral
galaxies: starburst
galaxies: star clusters: general

galaxies: star clusters: individual: . . .
galaxies: star formation
galaxies: statistics
galaxies: stellar content
galaxies: structure

Cosmology
(cosmology:) cosmic background radiation
(cosmology:) cosmological parameters
(cosmology:) dark ages, reionization, first stars
(cosmology:) dark energy
(cosmology:) dark matter
(cosmology:) diffuse radiation
(cosmology:) distance scale
(cosmology:) early Universe
(cosmology:) inflation
(cosmology:) large-scale structure of Universe
cosmology: miscellaneous
cosmology: observations
(cosmology:) primordial nucleosynthesis
cosmology: theory

Resolved and unresolved sources as a function of wavelength
gamma-rays: diffuse background
gamma-rays: galaxies
gamma-rays: galaxies: clusters
gamma-rays: general
gamma-rays: ISM
gamma-rays: stars
infrared: diffuse background
infrared: galaxies
infrared: general
infrared: ISM
infrared: planetary systems
infrared: stars
radio continuum: galaxies
radio continuum: general
radio continuum: ISM
radio continuum: planetary systems
radio continuum: stars
radio continuum: transients
radio lines: galaxies
radio lines: general
radio lines: ISM
radio lines: planetary systems
radio lines: stars
submillimetre: diffuse background
submillimetre: galaxies
submillimetre: general
submillimetre: ISM
submillimetre: planetary systems
submillimetre: stars
ultraviolet: galaxies
ultraviolet: general
ultraviolet: ISM
ultraviolet: planetary systems
ultraviolet: stars
X-rays: binaries
X-rays: bursts
X-rays: diffuse background
X-rays: galaxies
X-rays: galaxies: clusters
X-rays: general
X-rays: individual: . . .
X-rays: ISM
X-rays: stars

Transients
(transients:) black hole mergers
(transients:) black hole - neutron star mergers
(transients:) fast radio bursts
(transients:) gamma-ray bursts
(transients:) neutron star mergers
transients: novae
transients: supernovae
transients: tidal disruption events